Evidence for a 36 ks phase modulation in the hard X-ray pulses from the magnetar 1E 1547.0−5408

Kazuo Makishima,[1,2,3,*] **Teruaki Enoto,**[4,5,6] **Hiroaki Murakami,**[1] **Yoshihiro Furuta,**[1] **Toshio Nakano,**[1,2] **Makoto Sasano,**[1] **and Kazuhiro Nakazawa**[1,2]

[1]Department of Physics, The University of Tokyo, 7-3-1 Hongo, Bunkyo-ku, Tokyo 113-0033, Japan

[2]Research Center for the Early Universe, The University of Tokyo, 7-3-1 Hongo, Bunkyo-ku, Tokyo 113-0033, Japan

[3]MAXI Team, The Institute of Physics and Chemical Research (RIKEN), 2-1 Hirosawa, Wako, Saitama 351-0198, Japan

[4]High Energy Astrophysics Laboratory, RIKEN Nishina Center, 2-1 Hirosawa, Wako, Saitama 351-0198, Japan

[5]The Hakubi Center for Advanced Research, Kyoto University, Yoshida Ushinomiya-cho, Sakyo-ku, Kyoto, Kyoto 606-8302, Japan

[6]Department of Astronomy, Kyoto University, Kitashirakawa-Oiwake-cho, Sakyo-ku, Kyoto, Kyoto 606-8502, Japan

*E-mail: maxima@phys.s.u-tokyo.ac.jp

Abstract

The Suzaku data for the highly variable magnetar 1E 1547.0−5408, obtained during the 2009 January activity, were reanalyzed. The 2.07 s pulsation, detected in the 15–40 keV HXD data, was found to exhibit phase modulation, which can be modeled by a sinusoid with a period of $36.0^{+4.5}_{-2.5}$ ks and an amplitude of 0.52 ± 0.14 s. While the effect is also seen in the 10–14 keV XIS data, the modulation amplitude decreased towards lower energies, becoming consistent with 0 below 4 keV. After the case of 4U 0142+61, this makes the second example of this kind of behavior detected from magnetars. The effect can be interpreted as a manifestation of torque-free precession of this magnetar, which is suggested to be prolately deformed under the presence of a strong toroidal field of $\sim 10^{16}$ G.

Key words: stars: individual: 1E 1547.0−5408 — stars: magnetars — stars: magnetic fields — stars: neutron

1 Introduction

Magnetars (e.g., Thompson & Duncan 1995; Mereghetti 2008) are considered to be magnetically powered isolated neutron stars (NSs) having ultra-strong dipole magnetic fields, $B_{\rm d} = 10^{14-15}$ G, as derived from their pulse periods P and period derivatives $\dot{P}$. These values of $B_{\rm d}$ exceed

the so-called critical field, 4.4×10^{13} G, above which the Landau level separations of electrons exceed their rest-mass energy. Magnetars emit characteristic two-component X-ray spectra, consisting of the long-observed soft component and the mysterious hard component (Kuiper et al. 2006; den Hartog et al. 2006; Enoto et al. 2010b).

Magnetars are thought to harbor even higher *toroidal* (or internal) magnetic fields B_t (e.g., Thompson & Duncan 1995; Harding & Lai 2006; Braithwaite 2009; Dall'Osso et al. 2009). These fields may be generated and amplified in the progenitor's core, during its final gravitational collapse involving strong differential rotation (e.g., Takiwaki et al. 2009). Some models explain the production of energetic particles in magnetars by invoking toroidal magnetic fields and the associated twisted magnetic configuration (e.g., Beloborodov et al. 2007).

Observationally, the presence of intense B_t is supported by the recently discovered low-B_d magnetars, SGR 0418+5729 (Rea et al. 2013), SGR 1822−1606 (Rea et al. 2012), and 3XMM J185246.6+003317 (Rea et al. 2014); their burst activity suggests that their internal fields are much stronger than their externally observable fields of $B_d = 6 \times 10^{12}$ G, 2.7×10^{13} G, and $<1.4 \times 10^{13}$ G, respectively. The possible proton cyclotron feature in SGR 0418+5729, which suggests a local surface field of $>2 \times 10^{14}$ G (Tiengo et al. 2013), provides more support, because a portion of such intense internal fields would emerge from the NS surface to form local multipoles. Thus, the strong B_t may be regarded as one of the most important properties of magnetars. However, it remained difficult to more directly estimate B_t, because toroidal fields are intrinsically confined inside the NS and invisible from outside.

After pioneering works by, for example, Carlini and Treves (1989) and Heyl and Hernquist (2002), the way around this difficulty was explored by Makisihma et al. (2014, hereafter MEA14) in the following way. When an NS has $B_t \sim 10^{16}$ G, it is expected to be deformed into a prolate shape (Ioka 2001; Cutler 2002; Iokai & Sasaki 2004), to a degree of

$$\epsilon \equiv (I_1 - I_3)/I_3 \sim 1 \times 10^{-4}(B_t/10^{16}\,\text{G})^2, \tag{1}$$

where I_3 is the moment of inertia around the NS's symmetry axis $\hat{x}_3$, and I_1 that around axes orthogonal to $\hat{x}_3$. Under the absence of external torque, such an NS has a constant rotation period $P_{\text{rot}} \equiv 2\pi I_3/L$ around $\hat{x}_3$, and a constant precession period $P_{\text{prec}} \equiv 2\pi I_1/L$ around the angular momentum vector $\vec{L}$ (with $L \equiv |\vec{L}|$) which is fixed to the inertial frame. These two periods, which were degenerate when spherical, thus become different just by ϵ. If $\hat{x}_3$ is tilted from $\vec{L}$ by a non-zero *wobbling angle* α, the NS is said to exhibit *free precession*, which is the most basic behavior of a torque-free rigid body with an axial symmetry (Landau & Lifshitz 1976; Butikov 2006). This concept should be distinguished from the more familiar *forced precession* driven by external torque, as seen in spinning tops.

Suppose that a precessing NS has a radiation pattern that breaks axial symmetry around $\hat{x}_3$. Then, as argued by

MEA14, the observed pulses will be phase modulated at the beat period between P_{rot} and P_{prec}, which is called the *slip period* and is given as (assuming $\cos\alpha \sim 1$)

$$T \equiv P_{\text{prec}}/\epsilon = (1/P_{\text{rot}} - 1/P_{\text{prec}})^{-1}. \tag{2}$$

Using the Suzaku X-ray observatory (Mitsuda et al. 2007), MEA14 in fact found that the $P = 8.687$ s pulsation of the spectral hard component of the magnetar 4U 0142+61 is subject to phase modulation with a period of $T = 55 \pm 4$ ks. When this effect is interpreted as a manifestation of free precession and T is identified with the associated slip period, equation (2) yields $\epsilon = 1.6 \times 10^{-4}$, and hence equation (1) implies $B_t \sim 10^{16}$ G. This provides one of the first direct estimations of B_t for a magnetar.

As seen above, the essential assumptions made by MEA14 to interpret the observed phase modulation of 4U 0142+61 are: $\epsilon \neq 0$, $\alpha \neq 0$, and the broken axial symmetry of the hard X-ray emission pattern around $\hat{x}_3$. If these assumptions generally hold in objects of this class, we should observe the same effects from other magnetars as well. If detected from a reasonable number of them, the effect will provide such important information as how B_t is distributed among them, whether B_d and B_t are correlated, and whether B_t actually decreases (as postulated in the magnetar scenario itself: Thompson & Duncan 1995) towards objects with larger characteristic ages. The results will also provide valuable clues to the origin of the hard X-ray component (Kuiper et al. 2006; den Hartog et al. 2006), to the nature of the intriguing spectral evolution of magnetars discovered by Enoto et al. (2010b), and to the ultimate origin of these mysterious objects (e.g., Vink & Kuiper 2006; Nakano et al. 2015). Thus, examining other magnetars for the hard X-ray phase modulation is extremely important and urgent.

In the present paper, we have chosen the highly variable magnetar 1E 1547.0−5408 as our second target. It is the fastest rotating magnetar with $P = 2.07$ s, possibly associated with the supernova remnant G327.24−0.13 (Gelfand & Gaensler 2007). The observed value of $\dot{P} = 2.4 \times 10^{-11}$ s s^{-1} (Kuiper et al. 2012), together with P, yields $B_d = 2.2 \times 10^{14}$ G and a very young characteristic age of $\tau \equiv P/2\dot{P} = 1.4$ kyr. On 2009 January 22, strong bursting activity was detected from 1E 1547.0−5408 with Swift (Gronwall et al. 2009). This activity was continuously covered by RXTE, INTEGRAL, and Swift observations (Kuiper et al. 2012). These monitoring studies revealed an increase in the total flux at the burst onset by more than an order of magnitude, followed by a rapid decline, and complex changes in the spin-down characteristics along the activity evolution.

As already reported by Enoto et al. (2010a), hereafter Paper I, and Enoto et al. (2012), this object was observed by Suzaku during its 2009 January outburst, and yielded by far the strongest hard X-ray ($>10\,\mathrm{keV}$) signals among some ten magnetars so far observed with Suzaku. Although this source was observed with Suzaku again on 2010 August, these follow-up data are not utilized here, since the source had faded by that time in hard X-rays to a level comparable to the HXD detection limit (Iwahashi et al. 2013).

2 Observation

As described in Paper I and Enoto et al. (2012), the present Suzaku observation of 1E 1547.0−5408 was performed from 2009 January 28 21:34 (UT) to January 29 21:32 (UT), for a gross duration of 86 ks, with the target placed at the HXD nominal position. This was a Target of Opportunity observation in response to the activity onset, and this epoch falls in "segment 3" (from 2009 January 22 to February 1) of Kuiper et al. (2012). Among the three operating cameras of the X-ray Imaging Spectrometer (XIS: Koyama et al. 2007), XIS 0 was operated in the timing mode (P-sum mode), with a 7.8 ms time resolution. The Hard X-ray Detector (HXD: Takahashi et al. 2007) was operated in the standard mode, yielding a time resolution of 61 μs. Further details of the observation are found in Paper I.

Below, we mainly utilize the data from XIS 0 and HXD-PIN processed as described in Paper I, in which each detected event is tagged with the energy and the arrival time. Those from XIS 1 and XIS 3 had too low a time resolution (2.0 s) to resolve the pulsation, and signal statistics were rather low in HXD-GSO. The net exposure achieved with XIS 0 was 42.6 ks, while that with the HXD was 33.5 ks. After subtracting the background and applying dead-time corrections, the object was detected with HXD-PIN at a 15–70 keV count rate of $0.174 \pm 0.004\,\mathrm{counts\,s^{-1}}$ (Paper I), and a 1–10 keV rate of $5.5 \pm 0.1\,\mathrm{counts\,s^{-1}}$ with XIS 0.

As described in Paper I, 13 short-burst candidates were removed, and arrival times of the XIS 0 and HXD-PIN events were photon-by-photon converted to those to be measured at the solar system barycenter. The conversion utilized the source position of $(\alpha^{2000.0}, \delta^{2000.0}) = (15^{\mathrm{h}}50^{\mathrm{m}}54\overset{\mathrm{s}}{.}11, 54°18'23\overset{''}{.}7)$, as well as the spacecraft orbital information.

3 Data analysis and results

3.1 Reconfirmation of Paper I

Since the present paper reanalyzes the same data set of 1E 1547.0−5408 as used in Paper I, let us begin by reproducing the timing results of that publication. While Paper I utilized the conventional chi-square method to search for the pulsations, here we instead employ the Z_n^2 technique (Buccheri et al. 1983; Brazier 1994) which is free from the ambiguity of phase-bin number per pulse cycle and is generally less affected by the Poisson errors. For each trial pulse period P, this technique effectively calculates the folded pulse profile using a sufficiently large bin number (in practice not specified). Then, the Fourier power of the profile is summed up to a specified harmonic number n ($n = 1, 2, \ldots$), and normalized in a certain manner to reflect the data statistics. This process yields the statistical quantity called Z_n^2, which evaluates the significance of periodicity at P. If no intrinsic periodicity is present at P except Poissonian fluctuations, the Z_n^2 value calculated according to the normalization of Brazier (1994), which we adopt here, should obey a chi-square distribution with $2n$ degrees of freedom. The higher noise tolerance of this technique is realized by discarding the power in all harmonics higher than is specified.

Figure 1a shows periodograms calculated in this way using the 2–10 keV XIS 0 data and the 12–70 keV HXD-PIN data, both including backgrounds. The harmonic number was chosen to be $n = 2$, considering the double-peaked pulse profile of this source (e.g., Paper I). These energy bands, as well as the trial period range (2.0713–2.0730 s), are the same as those in Paper I, while the employed period search step, 1×10^{-6} s, is four times finer. The results reconfirm essential features of figure 3 of Paper I, including the best-estimate period of

$$P_{0\mathrm{s}} = 2072.135 \pm 0.005\,\mathrm{ms} \tag{3}$$

referring to the XIS result, and the side lobe patterns. The HXD periodogram peak,

$$P_{0\mathrm{h}} = 2072.147 \pm 0.005\,\mathrm{ms}, \tag{4}$$

is consistent with equation (3) within errors, although it is slightly displaced to longer periods. This behavior is also seen in figure 3 of Paper I. The errors in $P_{0\mathrm{s}}$ and $P_{0\mathrm{h}}$ refer to the range where pulse-phase differences amount to $\pm 10\%$ of one pulse cycle when accumulated over the gross duration of 86 ks. These errors approximately agree with the widths of the peaks in the periodograms.

At $P_{0\mathrm{h}}$, the 12–70 keV HXD periodogram in figure 1a reaches the peak height of $X = 28.21$, where Z_2^2 is abbreviated to X. In terms of the chi-square distribution with $2n = 4$ degrees of freedom, the chance probability of finding X values higher than this is found as $\mathcal{P}_2^{\mathrm{h}} = 1.1 \times 10^{-4}$; here, the subscript specifies the harmonic number n, and the superscript "h" means the HXD. This agrees with the probability of $\sim 1 \times 10^{-4}$ obtained in Paper I for 10–70 keV with the chi-square technique.
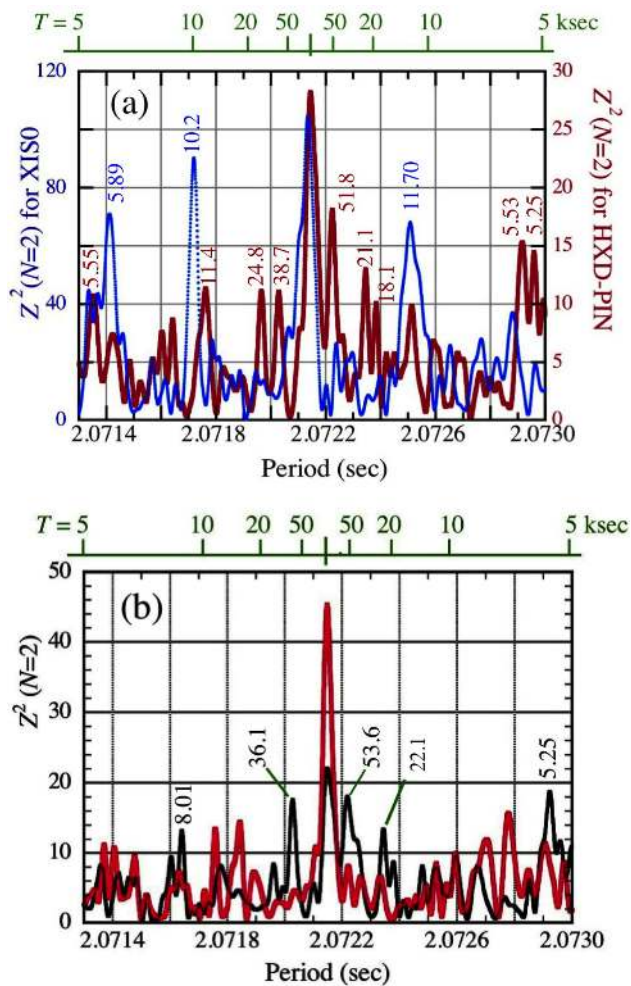
Fig. 1. (a) Periodogram of 1E 1547.0−5408 calculated using the Z_n^2 method with $n = 2$, from the 2–10 keV XIS 0 data (blue) and those of HXD-PIN in 12–70 keV (brown). (b) As panel (a), but for the 15–40 keV HXD-PIN data, before (black) and after (red) applying the demodulation analysis employing the parameters of equation (10). In both panels, the green abscissa at the top indicates the period T which can explain a side lobe at that period in terms of its beat with the pulsation. The implied values of T (in units of ks) of major side lobes are also indicated in the figure.

In figure 1a, the XIS and HXD periodograms both show a number of side lobes. Such a structure at a period P' often arises due to beat between the pulsation at P_0 (representing P_{0s} or P_{0h}) and a certain longer period T. Based on this assumption, we calculated the required period as $T = |(1/P_0 - 1/P')^{-1}|$, and show it in green at the top of figure 1. In addition, the required values of T (in units of ks) of major XIS 0 and HXD side lobes are given explicitly in the figure. Thus, many of the side lobes (particularly of XIS 0) in figure 1a can be explained as a beat of P_0 with $T = 5$–6 ks or $T = 10$–12 ks, which agree with Suzaku's orbital period $P_{\rm orb} = 5.6$ ks or twice this value, respectively. However, the HXD-PIN periodogram shows several unexplained peaks: at $T = 24.8$ ks and 38.7 ks on the

left side of P_0, as well as at $T = 51.8$ ks, 21.1 ks, and 18.1 ks on the right side. These structures, also seen in figure 3 of Paper I, suggest that the hard X-ray pulses could be affected by some long periodicity in the range $T = 18$–52 ks (5.0–14.4 hr).

3.2 Detailed analysis of the HXD data

Below, we analyze the HXD-PIN data in further detail, selecting an energy range of 15–40 keV. The lower energy bound is thus raised from the 12 keV used in figure 1a to 15 keV, to avoid increased soft thermal noise. Likewise, the upper energy bound is lowered from 70 keV to 40 keV, to reduce the contribution from the non-X-ray background.

3.2.1 Evolution of hard X-ray pulse profiles

The Z_2^2 periodogram calculated from the 15–40 keV HXD-PIN data is shown in figure 1b in black. Apart from some small differences, it is similar to the 12–70 keV results shown in brown in panel (a). The peak value, also obtained at the period of equation (4), becomes

$$X_0 \equiv (X)_{A=0} = 22.06, \tag{5}$$

which is somewhat smaller than that in 12–70 keV.

In the 15–40 keV periodogram, the period range of $T = 18$–52 ks, where the unexplained side lobes were noticed in figure 1a, is approximately preserved (although the detail of the side lobes is changed). Since this period range does not contain particular artificial periodicities of the observation such as data gaps or background variations, some properties (e.g., amplitude, phase, or pulse shapes) of the 2.07 s hard X-ray pulsation could be subject to slow variations with periods in this range. In fact, Kuiper et al. (2012) found that the pulse shapes were changeable during their "segment 3" which covers the present Suzaku observation, that a new intermediate peak in the >4 keV pulse profile emerged, and that the pulsed hard X-ray flux *increased* even though the total 4–27 keV flux was rapidly declining.

To examine the evolution of the hard X-ray pulse properties, we divided the whole observation into consecutive time segments of approximately equal lengths, denoted by $j = 0, 1, \ldots, J-1$, and sorted the entire 15–40 keV HXD-PIN events (including backgrounds) into a two-dimensional array $C(j, k)$. Here, the column $k = 0, 1, \ldots, K-1$ represents the pulse phase (i.e., the photon arrival times modulo P_{0h}). Thus, a set $\{C(j, k); k = 0, \ldots, K-1\}$ gives the pulse profile in the jth time segment. We employed $J = 6$ and $K = 12$, and show in figure 2a the obtained time-divided six pulse profiles as a function of k. There, running averages were applied to three consecutive data points ($k-1$, k, $k+1$). Thus, the pulse amplitude changes
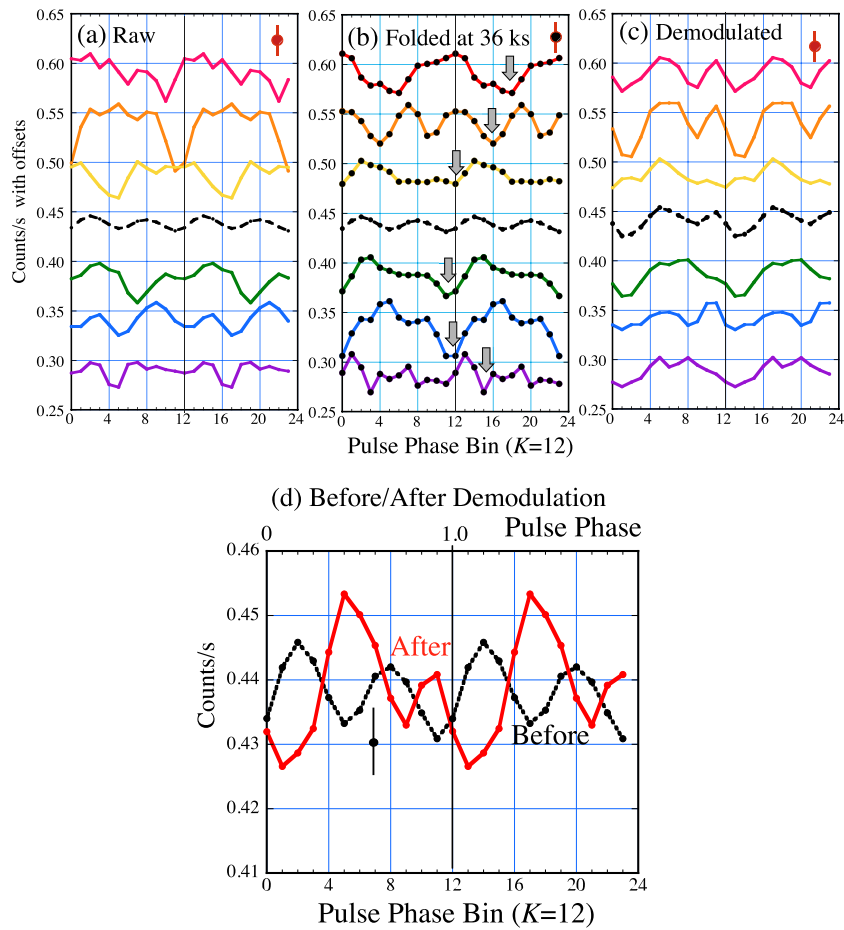
Fig. 2. (a) The 15–40 keV background-inclusive pulse profiles folded at equation (4), obtained in six consecutive time segments of ∼14 ks each (from red to purple). They are shown for two cycles, with vertical offsets, after applying running averages over three adjacent bins. A typical $\pm 1\sigma$ statistical error is given at the top right corner. The dashed black profile at the middle represents the average. (b) The 15–40 keV folded pulse profiles accumulated over six different phases of the $T = 36$ ks modulation period, shown with offsets. The meaning of the colors is different from that in panel (a). A possible phase assignment is indicated by arrows. (c) As panel (a), but prior to the folding, the arrival time of each event was corrected with equation (8) using the parameters of equation (10). (d) A comparison between the 15–40 keV pulse profiles before (black) and after (red) the demodulation, both with the running averages. The former is the same as the black profiles in panels (a) and (b), while the latter is identical to the black one in panel (c). The background level is at about 0.27 counts s^{-1}.

with time, and the pulse shape is also variable; it is relatively flat-topped with a single deep minimum, and an occasional shallower secondary minimum at about half a cycle offset. Such a short-term variation in the pulse shape was observed from 4U 0142+61 (Enoto et al. 2011), as well as from 1E 1547−5408 itself (Kuiper et al. 2012).

More importantly, thanks to the high sensitivity of the Suzaku HXD on relatively short time scales (Kokubun et al. 2007), the pulse *phase* is seen to vary clearly in figure 2a, by up to about half a pulse cycle. On the other hand, we do not notice in figure 2a particular *secular* changes in the pulse profile, pulsed flux, or pulse phase. This does not contradict the discovery by Kuiper et al. (2012) of the emerging new component in the hard X-ray pulse profile, because the growth of that component is estimated to be at most ∼10% across the present Suzaku pointing, as judged from the

history of the hard X-ray pulsed flux (figure 9 of Kuiper et al. 2012).

3.2.2 Periodic phase modulation

We next need to know whether the pulse-phase fluctuations seen in figure 2a are *periodic* or not. This requires a finer time division by increasing J, but individual pulse profiles would then lose statistics. Therefore, we chose another way; the data accumulation was repeated with $J = 20$ and $K = 5$, but the results are presented in figure 3a in the form of five *light curves*, $\{C(j, k); j = 0, \ldots, J = 19\}$ using j as abscissa. For presentation, three-point running averages were again applied over $(j - 1, j, j + 1)$. Thus, the background-inclusive count rates in the five pulse phases mostly varied rather periodically, by
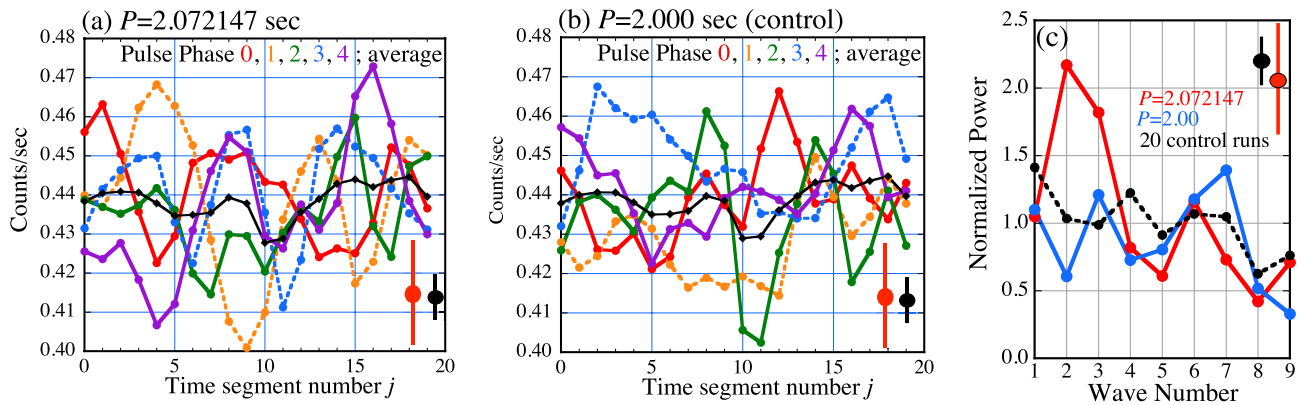
Fig. 3. (a) Background-inclusive 15–40 keV light curves of 1E 1547.0−5408, each covering the entire observation with 20 segments ($j = 0, 1, \ldots, 19$), derived in five different phases (red, orange, green, blue, and purple) of the pulse period of equation (4). See text for details. They are shown after applying a running average over the adjacent three bins, and their average is given by the solid black line. Typical $\pm 1\,\sigma$ error bars are given at the bottom right corner. (b) The same as panel (a), but sorted into five phases of a dummy period of 2.0 s. (c) Power spectra of the five light curves in panels (a) and (b), in red and blue lines, respectively. Both are normalized to the power expected from the Poisson fluctuations. The black dashed line represents an ensemble average over 20 control studies, each similar to panel (b).

two to three cycles across the 86 ks gross pointing, although the amplitude is comparable to the statistical errors.

We calculated discrete Fourier power spectra of the five light curves in figure 3a, before taking the running averages, and summed them to obtain a single power spectrum which is shown by a red solid line in figure 3c. It indeed reconfirms the suggested power enhancement, at wave numbers of $q = 2$ and $q = 3$, with the corresponding period range of

$$86/3 = 29\,\text{ks to } 86/2 = 43\,\text{ks}. \tag{6}$$

The weighted mean of $q = 2$ and $q = 3$ over the power spectrum in figure 3c becomes

$$q = 2.45, \text{ or } T = 35.1\,\text{ks}, \tag{7}$$

which is fully consistent with the implication of the side lobes in figure 1.

As a "control" study, figure 3b presents another set of light curves, calculated in the same way but purposely changing the folding period from P_0 to a dummy value of 2.0 s. Its behavior is clearly more random, without particularly favored periods. Indeed, these five control light curves yielded the blue power spectrum in figure 3c, which is consistent with white noise.

To evaluate the significance of the $q = 2$ and $q = 3$ enhancements in the red power spectrum of figure 3c, we repeated the same control study 20 times, by changing the dummy period around 2.0 s. The derived ensemble-averaged power spectrum, shown in figure 3c by a dashed black line, is approximately white (with hints of red noise at $q = 1$ and background variation at $q = 4$ corresponding to $5P_{\text{orb}}$). Around this mean, individual power spectra exhibited a $1\,\sigma$ scatter by $\sim \pm 0.5$. Therefore, the $q = 2$ and

$q = 3$ excess (above 1.0) in the red power spectrum is estimated to be 2.4 and 1.6 sigma effects, and their sum implies a ~ 3 sigma excess.

Since the five light curves in figure 3a do not vary in phase, the suggested long periodicity is unlikely to result from pulse-amplitude variations, but are considered to reflect the pulse-phase jittering found in figure 2a. Thus, the hard X-ray pulsation is inferred to exhibit *periodic phase modulation*. To reinforce this inference, we accumulated the pulse profiles in six separate phases of an assumed periodicity of $T = 36$ ks, of which the choice is justified later. The result is presented in figure 2b; in this case, the row j of the array $C(j, k)$ denotes the pulse phase, i.e., the arrival times modulo T, rather than the arrival times themselves. It shows a periodic and approximately sinusoidal pulse-phase modulation, with an amplitude of $\Delta k \sim \pm 3.5$ bins (± 0.3 pulse cycle or ± 0.6 s) which is consistent with the inference from figure 2a.

3.2.3 Demodulation analysis

The above semi-quantitative analysis justifies our applying the "demodulation analysis," developed by MEA14, to the HXD data, to more rigorously quantify the pulse-phase modulation. Specifically, we consider that the hard X-ray pulsation of 1E 1547.0−5408 is somehow phase modulated, like in 4U 0142+61, at a period T in the range of equation (6). We hence assume that the peak timing t of each 2.07 s pulse is displaced sinusoidally by

$$\Delta t = A \sin(2\pi t / T - \phi), \tag{8}$$

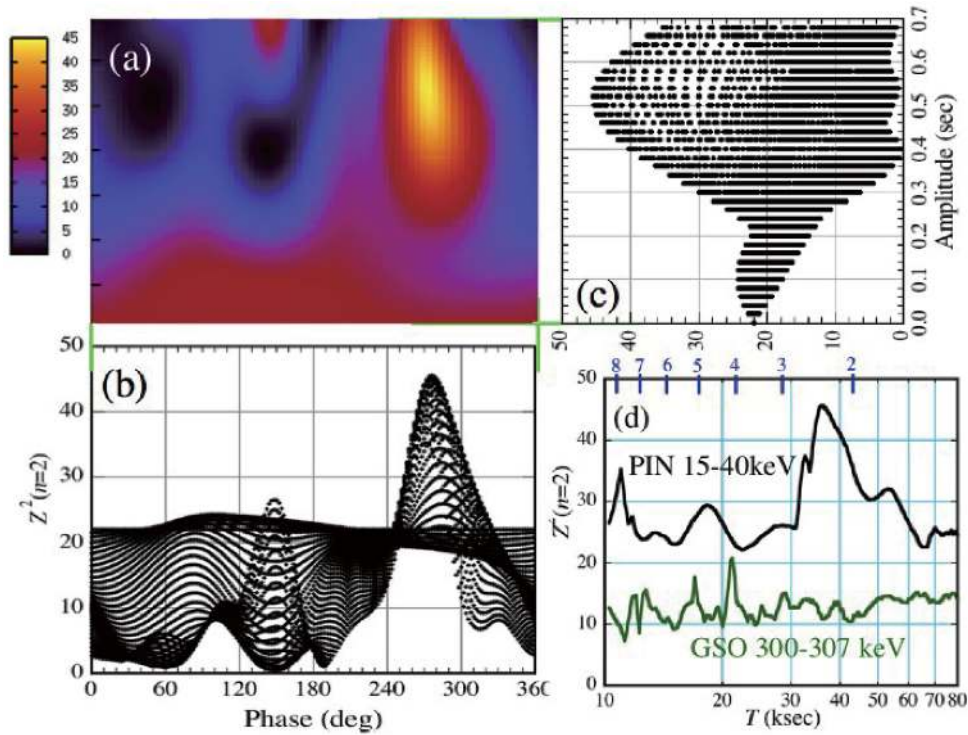where A and ϕ are the amplitude and initial phase of the assumed modulation, respectively.

Fig. 4. Results of the demodulation analysis on the 15–40 keV HXD-PIN data, assuming a periodic phase modulation described by equation (8). (a) A two-dimensional color map of $X \equiv Z_2^2$ (maximum as P is varied) on the (A, ϕ) plane, assuming $T = 36.0$ ks. (b) Projection of panel (a) onto the ϕ axis. (c) Projection onto the A axis. (d) T-dependence of the Z_2^2 peak value, $X_{pk}(T)$, presented in black. Green shows a reference result using the 300–307 keV HXD-GSO data. The corresponding Fourier wave number, for the total time span of 86 ks, is shown in blue at the top.

As formulated in MEA14, such effects can be removed by shifting the arrival times of individual HXD photons back by $-\Delta t$. This procedure was previously employed, e.g., by Koyama et al. (1989) to search for orbital motions in the anomalous X-ray pulsar 1E 2259+586, and by Terada et al. (2008) to remove the orbital effects in the fastest-spinning accreting white dwarf binary, AE Aqr, and successfully detect its hard X-ray pulsations. We hence applied these time displacements to the individual HXD photons, and recalculated the Z_2^2 periodograms to see whether the pulse significance changes. The pulse period was scanned over a range of $P = 2.072130$–2.072152 (with a step $1\,\mu$s), i.e., the joint error range of equations (3) and (4). The triplet (T, A, ϕ) describing the phase modulation was scanned over $A = 0$–0.80 s (with a 0.05 s step), $\phi = 0°$–$360°$ ($3°$–$10°$ step), and $T = 10$–80 ks (with a step of 0.2 to 0.5 ks). The harmonic number $n = 2$ is retained.

The results of this *demodulation* analysis are presented in figure 4, in just the same format as figure 2 of MEA14. Here, panel (a) shows a two-dimensional color map of the value of $X \equiv Z_2^2$ (the maximum as P is varied) obtained on each grid point (A, ϕ), for a particular case of $T = 36.0$ ks. Its projections on the ϕ and A axes are presented in panels (b) and (c), respectively, where multiple traces indicate cross sections of panel (a) at various

positions. While the value of X_0 in equation (5) is reproduced at $A = 0$ in panel (c), a clear peak is seen at $A \sim 0.52$ s and $\phi \sim 270°$. This value of A agrees well with what can be read from figure 2b. Furthermore, the value of ϕ, together with equation (8), predicts $\Delta t = +A$ (the maximum delay) at about the beginning ($t \sim 0$) of the $T = 36$ ks phase, again in agreement with figure 2b. Although figure 2a apparently suggests a rather long periodicity (e.g., $T > 100$ ks), this is probably a beat between the $T = 36$ ks modulation and the Nyquist period therein ($1 \times 86/6 = 29$ ks), which should appear at 140 ks.

In panels (a)–(c) of figure 4, the peak significance reaches $X_{pk} = 45.60$; here, $X_{pk}(T)$ denotes the peak value of X found on the (A, ϕ) plane for a given value of T. Panel (d) of figure 4 shows how this $X_{pk}(T)$ depends on the assumed modulation period T. Over the entire (P, T, A, ϕ) space surveyed, the highest value of X, to be called the grand-maximum and denoted X_{max}, is thus found to be

$$X_{max} \equiv X_{pk}(36.0\,\text{ks}) = 45.60, \tag{9}$$

for a set of modulation parameters given as

$$A = 0.52 \pm 0.14\,\text{s}, \quad \phi = 276° \pm 15°, \quad T = 36.0^{+4.5}_{-2.5}\,\text{ks}. \tag{10}$$

Here, the errors are represented in the same way as in MEA14, i.e., by the standard deviations of Gaussians fitted to the distributions (above uniform backgrounds) in figure 4. This value of T, already employed to produce figure 2b, agrees well with equation (7).

As shown in figure 1b in red, the demodulation with equation (10) has changed the HXD-PIN periodogram significantly. The peak at P_{0h} has become much higher, just from X_0 to X_{max}. Furthermore, the P_{orb}-unrelated side lobes have diminished; powers therein are thought to have been restored to the main peak.

In figure 2c, we again calculated the 15–40 keV folded pulse profiles in the same six time segments as in figure 2a, but after applying the time corrections by equation (8) to individual photons using the parameters in equation (10). Thus, the six consecutive profiles have indeed lined up in their phases. A small subpeak, just prior to the minimum, is seen in at least four out of the six profiles. These results reinforce the validity of the demodulation analysis. Figure 2d reproduces, and directly compares, the time-averaged 15–40 keV pulse profiles before and after the demodulation. Thus, the pulse amplitude has been nearly doubled.

3.2.4 Significance of the phase modulation
Although the phase demodulation procedure largely increased the HXD pulse amplitude (and hence the pulse significance), we need to examine whether this increase is statistically significant, or merely due to a chance superposition of Poisson noise of the data on the already existing pulse periodicity at P_{0h}.

The nominal chance probability of finding values of $X \geq X_{max}$ of equation (9) is extremely small, $\mathcal{P}_2^h = 3.0 \times 10^{-9}$. However, we cannot use this face value to evaluate the statistical significance of the detected effect, for the following two reasons.

(1) This $\mathcal{P}_2^h$ must be multiplied by the total number of *independent* trials involved in the computation of figure 4, but this quantity is not easy to estimate. The total number of parameter search steps actually employed would considerably overestimate this number, because the steps were chosen, rather arbitrarily, to be fine enough not to miss the X peaks.

(2) When evaluating the significance of X_{max}, we need to consider the fact that the HXD signals were already pulsing, before the demodulation procedure, at P_{0h} (Paper I) with a significance of $X_0 \gg n$. In addition, the variations in the pulse amplitude, profiles, and phase (figure 2) would contribute to X.

These two problems can be combined into a single question: when we scan over P, A, ϕ, and T, as in figure 4, what is the overall chance probability for the X statistics

to increase *by chance* from X_0 to X_{max} or higher when the source is pulsating with variable parameters but without any excess variation at T above the white noise?

To answer the above inquiry, we conducted 1000 simulation runs as detailed in the Appendix, using the actual 15–40 keV data themselves, but purposely randomizing, each time, the phase of the assumed 36 ks modulation: any white noise would not be affected by such randomization. Figure 5a shows a distribution of the grand-maximum value X_{max} obtained in this simulation study. It is considered to represent the probability distribution of X_{max}, to be found in the same demodulation analysis of the HXD data over the same (P, T, A, ϕ) space as figure 4, but under the absence of power enhancement (above white noise) at any T examined. There, values exceeding equation (9) were actually found in three out of the 1000 runs, namely, with a probability of 0.3%.

Figure 5b gives the upper integral probability associated with figure 5a. In the range of $X_{max} > 35$, it is approximated by an exponential as

$$f(> X_{max}) = f_0 \exp\left(-\frac{X_{max} - 40}{g_0}\right), \tag{11}$$

with $f_0 = 0.038 \pm 0.005$ and $g_0 = 2.2 \pm 0.2$, where $X_{max} = 40.0$ was chosen as a reference pivot point. The value of g_0 is consistent with the exponential factor, 2.0, that is expected for a chi-square distribution of any degree of freedom. Thus, a value of X_{max} which is equal to or larger than equation (9) will appear with a chance probability of

$$f(45.60) = (3 \pm 1) \times 10^{-3}, \tag{12}$$

in good agreement with the implication of panel (a). As noted in the Appendix, this estimate is considered rather conservative.

Considering that MEA14 used $n = 4$, it may be interesting to examine what happens if different values of n are employed. We hence repeated the same analysis with $n = 1$, 3, and 4, to find $X_{max} = 25.64$, 47.06, and 49.92, respectively. The optimum parameters were not much different from those in equation (10). Although the larger harmonic numbers somewhat increased X_{max} from equation (9), the effect is not significant considering the increased degree of freedom. In fact, the implied chance occurrence probability, $\mathcal{P}_1^h = 2.8 \times 10^{-6}$, $\mathcal{P}_3^h = 1.8 \times 10^{-8}$, and $\mathcal{P}_4^h = 4.2 \times 10^{-8}$, are all much higher than $\mathcal{P}_2^h$ obtained above, in agreement with the double-peaked pulse profiles. Therefore, we retain $n = 2$ below.

In short, we can exclude, at >99.6% confidence, the possibility that X_{max} of equation (9) in figure 4 arose via chance superposition of the photon count fluctuations on top of the hard X-ray pulsation of which the parameters
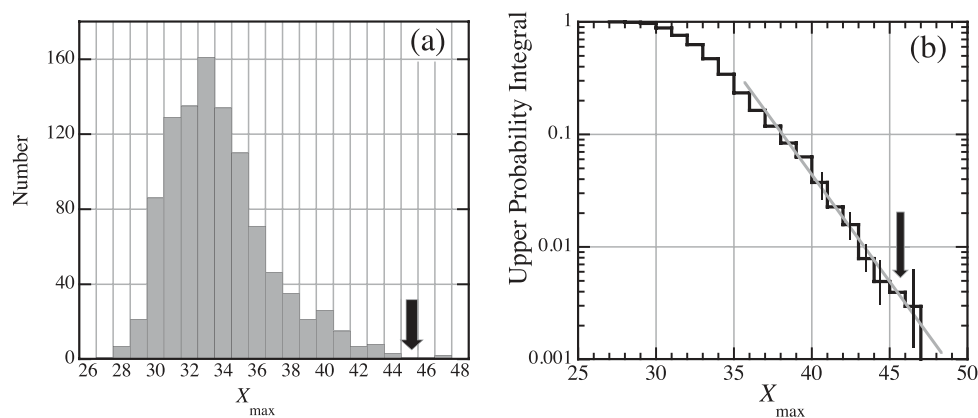
Fig. 5. A histogram of the values of X_{max} (panel a), and the associated upper probability integral (panel b), found in a series of 1000 simulation trials each equivalent to figure 4 but randomizing the 36 ks modulation phase. As described in the Appendix, it was derived from the data themselves. In both panels, a black arrow indicates equation (9).

vary with white noise. This confidence level is more stringent than the case of 4U 0142+61, where it was >99% (MEA14).

3.3 Analysis of the XIS data

The two-component spectral model, fitted in Paper I to the XIS+HXD spectrum of 1E 1547.0−5408, indicates that the soft thermal component and the hard power-law component cross over at ∼5 keV. Therefore, the hardest end of the XIS energy band, with its P-sum time resolution, is expected to provide independent information on the hard component, and allows us to cross-check the HXD-PIN results. (This was not feasible with 4U 0142+61, since the XIS was not operated in the P-sum mode in that observation.) To limit the soft-component contribution to <10%, we choose an energy range of 10–14 keV, and perform the same analysis as above. Although this energy range, which is in fact covered by the XIS, is seldom utilized in spectral studies mainly because of the calibration uncertainty therein, such problems do not affect timing studies.

Figure 6 shows the results of this demodulation analysis on the 10–14 keV XIS 0 data, presented in the same way as figure 4. Panels (a), (b), and (c) all refer to the condition of $T = 36.0$ ks after equation (10). On the (A, ϕ) plane, a clear peak with

$$X_{pk}(36 \text{ ks}) = 27.64 \tag{13}$$

is seen at a similar position to figure 4a. More specifically, A and ϕ can be constrained as

$$A = 0.46 \pm 0.11 \text{ s}, \quad \phi = 260° \pm 17°. \tag{14}$$

These values agree, within errors, with the corresponding results in equation (10). If the modulation parameters are

fixed to the best-fit values of equation (10) as determined with the HXD, we instead find

$$X_{pk}(36 \text{ ks}) = 17.08. \tag{15}$$

The demodulation with equation (14) has effects on the 10–14 keV periodograms as shown in figure 7a. While the value of $X \sim 5$ found before the demodulation (black) is within random fluctuations, a clear peak, of which the height is given by equation (13), appeared at a period that is in full agreement with equations (3) and (4).

Figure 7b shows 10–14 keV XIS 0 pulse profiles folded at P_{0s}, obtained using the demodulation parameters of equation (14) and presented in the same colors as in figure 2d. Again, the demodulation procedure significantly increased the pulse fraction. The red pulse profile is similar to that in figure 2d, although the relative depths of the two pulse minima are reversed. For reference, the 1–10 keV XIS 0 pulse profile is also shown.

The T-dependence of X_{pk} is shown in figure 6d. Thus, in addition to a small hump at $T = 36–38$ ks, we observe many other peaks, some being much higher. Among them, the sharp feature at $T \sim 11$ ks is likely to be caused by background variations, because it is close to $2P_{orb}$. Also, the plot reveals a prominent peak at $T = 44$ ks, which is probably due to a chance superposition of Poisson fluctuations on top of the demodulated pulsation. As a result, we cannot claim the presence of the $T = 36$ ks periodicity based on the XIS data alone. Nevertheless, the XIS results significantly reinforce the HXD-detected phase modulation: since the pulsation is insignificant in the raw periodogram (figure 7a), the probability of finding a peak of $X_{pk} = 17.08$ of equation (15) at the same (P, T, A, ϕ) point as specified by the HXD result can be directly evaluated with a simple chi-square distribution to be $\mathcal{P}_2^s = 1.9 \times 10^{-3}$.
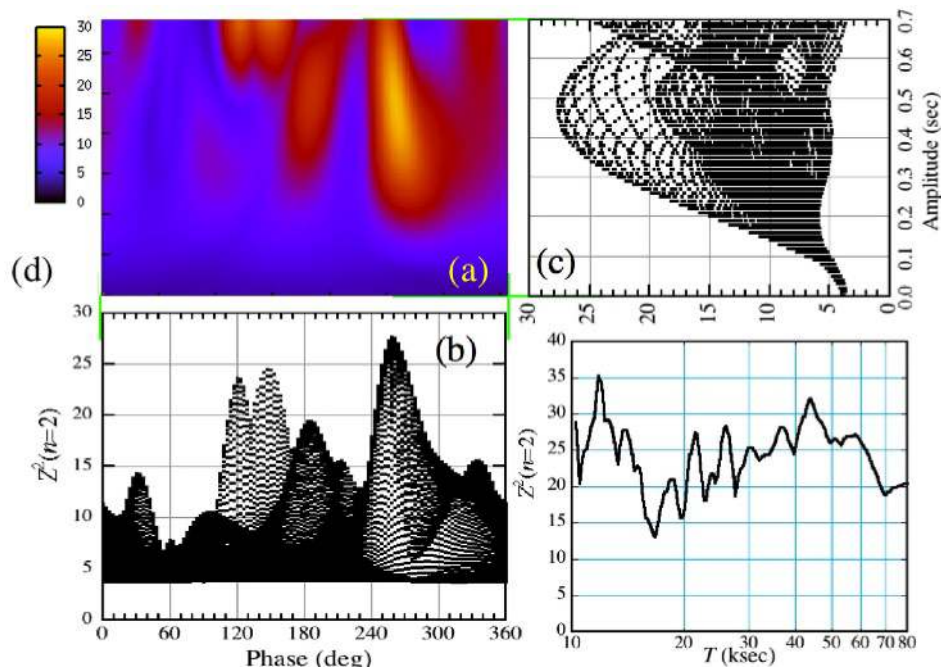
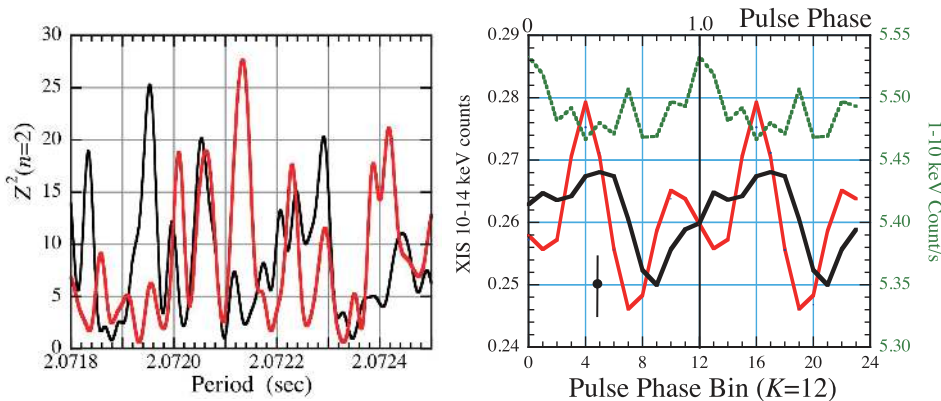**Fig. 6.** As figure 4, but using the 10–14 keV XIS 0 data.

Fig. 7. Effects of the demodulation on the 10–14 keV XIS 0 data. Equation (14) and $T = 36.0$ ks are employed. (a) Periodograms, before (black) and after (red) the demodulation. The plot is more expanded in the period range than those presented so far, to show finer details around the pulsation. (b) The 10–14 keV pulse profiles folded at $P = P_{0s}$, with the colors corresponding to those of panel (a). Running averages over the adjacent 3 bins are applied. The phase origin is the same as in figure 2. Green (with right ordinate) shows the 1–10 keV profile.

If we instead use equation (13), the probability further decreases to $\mathcal{P}_2^s = 1.5 \times 10^{-5}$.

3.4 Energy dependence of the modulation amplitude

Now that the 36 ks phase modulation in the hard X-ray pulses, first detected with the HXD, has been reinforced by the 10–14 keV XIS data, our next task is to examine how this phenomenon behaves towards lower energies. In the same way as above, we therefore analyzed the XIS 0 data in three lower energies: 7–10 keV, where the spectral hard component is still dominant; 4–7 keV, where they compete;

and 1–4 keV, dominated by the soft component. Figure 8 shows the results of this soft X-ray analysis, namely, scans in A in which $T = 36.0$ ks is fixed while ϕ is allowed to take any value. Thus, the 36 ks modulation amplitude clearly decreases towards lower energies, and the effect almost disappears in the 1–4 keV range.

Taking the 7–10 keV case as an example, we again calculated the 12-bin folded pulse profiles for six phases of $T = 36$ ks, in a similar manner to figure 2b. The result, shown in figure 8d, again shows the sinusoidal phase modulation, clearly with a smaller amplitude than in figure 2b. The amplitude can be read as $\Delta k / K \sim \pm 2/12 = \pm 0.17$ pulse phase, or $A = 0.17 P_{0h} = 0.35$ s, in good agreement with
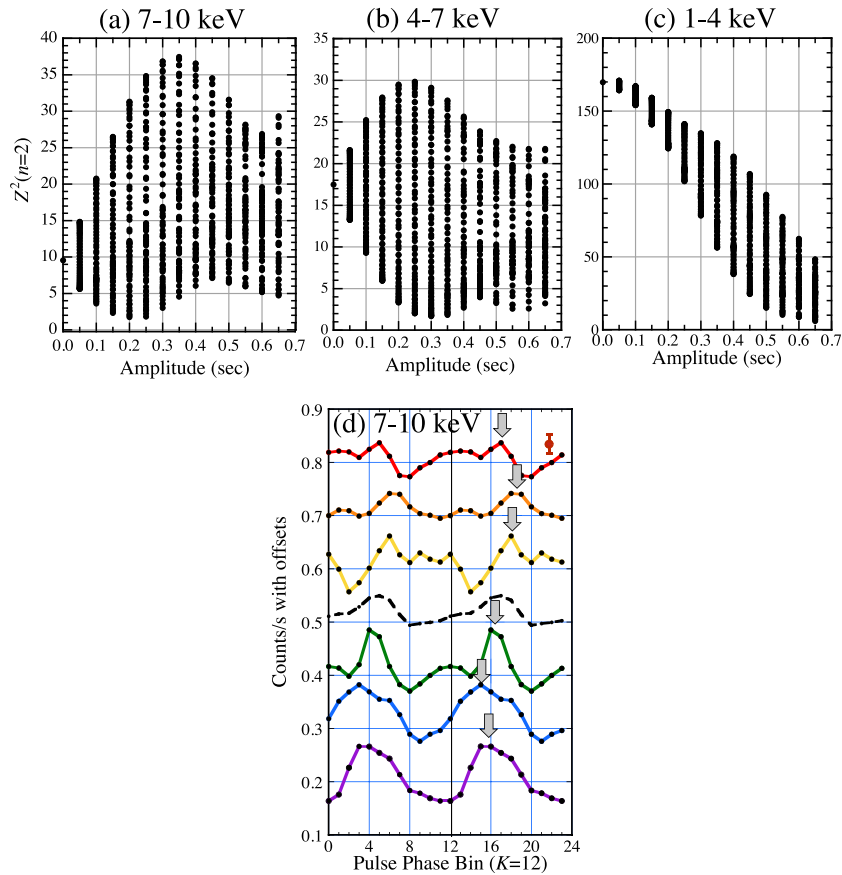
Fig. 8. (a) The same A-dependence of X as figure 4c and figure 6c, but for the 7–10 keV XIS 0 data. $T = 36$ ks is fixed, while ϕ is left free. (b) In 4–7 keV. (c) In 1–4 keV. (d) As figure 2b but for the 7–10 keV XIS 0 data. (Color online)
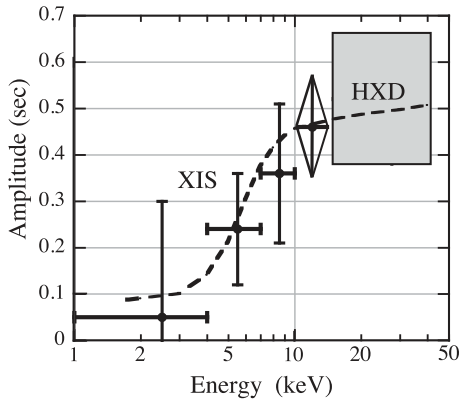

Fig. 9. The 36 ks phase modulation amplitude A, obtained at various energies with the HXD and the XIS. The modulation phase is not specified. The dashed curve represents equation (16).

figure 8a. In this case, the pulse peak is more clearly traced than the valley. Furthermore, the modulation phase is somewhat shifted from equation (10) to $\phi \sim 360°$.

Combining figure 8 with equations (10) and (14), the energy dependence of A is shown in figure 9. Here, the dashed curve represents the fractional contribution of

the hard component at that energy, namely

$$A = A_0 \times F_h / (F_s + F_h), \qquad (16)$$

where $A_0 = 0.5$ s is a fiducial amplitude at the hardest energy limit, while F_s and F_h are the intensities of the soft and hard components, respectively, according to the spectral decomposition (Model B) in Paper I. Interestingly enough, this empirical quantity behaves very similarly to the observed energy dependence of A, suggesting that the phase modulation is limited to the hard X-ray component.

Given figure 9, we attempted to divide the 15–40 keV HXD-PIN band into finer ranges, or to extend the analysis to higher energies beyond 40 keV up to $\sim$70 keV. However, due to limited statistics, the data provided no significant information on the possible energy dependence of the HXD phase modulation. Likewise, the HXD-PIN data below 15 keV (down to $\sim$10 keV) had such poor statistics that they did not allow us to cross-confirm the 10–14 keV XIS results. All that can be said is that the pulse-phase modulation in the HXD-PIN signal is consistent with being energy independent over the 10–70 keV range within rather large uncertainties.

3.5 Analysis of the HXD-GSO data

As described in Paper I, the signal from 1E 1547.0−5408 was marginally detected in the 60–100 keV range with HXD-GSO. Therefore, we analyzed the HXD-GSO data in various energy ranges from 50 to 200 keV, but the data gave significant evidence for neither the pulsation, nor its phase modulation. This is not surprising, because HXD-GSO has a considerably higher background than HXD-PIN (Kokubun et al. 2007).

Even though the HXD-GSO data provide no information on the source pulsation, they allow us to perform an important control study. We hence purposely chose a very high energy range, 300–307 keV, which is dominated by background and has nearly the same counting rate, 0.46 counts s^{-1}, as the background-inclusive 15–40 keV HXD-PIN rate (0.44 counts s^{-1}; figure 2). The green trace in figure 4d shows the derived X_{pk} behavior in this high energy band. Thus, the baseline value of $X_{pk} \sim 10$ is much lower than that in 15–40 keV, $X_{pk} \sim 22$, due to the absence of the pulsation. In addition, no peaks are observed around $T \sim 36$ ks. Since these HXD-GSO data were acquired by the same instrument as the HXD-PIN data, at exactly the same time, and under the same background conditions, the result argues against instrumental origins of the $T = 36$ ks periodicity in the 15–40 keV pulse phases.

4 Discussion

Through an extensive reanalysis of the Suzaku data of 1E 1547.0−5408 acquired in the 2009 outburst, we obtained evidence that the 2.07 s hard X-ray pulsation detected with the HXD is subject to phase modulation with a period of $T = 36$ ks (figure 4). Following the first detection from 4U 0142+61 ($P_0 = 8.69$ s, $T = 55$ ks, and $A \sim 0.75$ s; MEA14), this makes 1E 1547.0−5408 the second magnetar to exhibit this kind of evidence.

4.1 Trivial possibilities

4.1.1 Instrumental origin

The detected effect should first be examined for instrumental or observational artifacts. In sub-subsection 3.2.4, we excluded the statistical fluctuation origin at a 99.6% confidence level. Furthermore, the HXD-GSO data analysis (subsection 3.5) indicates that the HXD instrument does not suffer unexpected artifacts (e.g., background variations) that can explain away the X_{pk} maximum at $T = 36$ ks. The value of $T = 36.0$ ks $= 6.4 P_{orb}$ is not in harmonic resonance with Suzaku's orbital period, either.

In this respect, of particular importance is the cross-confirmation of the phase modulation with the 10–14 keV

XIS data (figure 6). This further rules out the possibility of the effect being due to some artifact specific to the HXD. Furthermore, the clear decrease of A towards lower energies (figure 9) excludes any instrumental or artificial origin specific to the overall Suzaku mission (e.g., unexpectedly large drifts in the spacecraft clock), because such effects should be independent of the photon energy. We are hence left with celestial interpretations.

4.1.2 Period derivatives

Based on figures 2b, 3a, and 3c, we have so far regarded the phase modulation as periodic, and performed the demodulation analysis to arrive at the modulation period of equation (10). However, the total data span, 86 ks, contains only 2.4 cycles of the 36 ks oscillation. Hence, we could be mistaking some other effects for the periodic phase changes.

One possibility is the period derivative, because magnetars generally spin down, presumably emitting magnetic dipole radiation. This will cause parabolic changes in the pulse phase, which could mimic a periodic phase modulation. From Entry No. 3 of table 4 in Kuiper et al. (2012), the average spin-down rate of 1E 1547.0−5408 is considered to be $\dot{P} \sim 2 \times 10^{-11}$ s s^{-1} around the present observation. Although this would cause a phase difference of only ~ 0.1 pulse cycle across the 86 ks length of the present data, there still remains a possibility that the instantaneous $\dot{P}$ was considerably higher.

With the above in mind, the Z_2^2 analysis was repeated on the 15–40 keV HXD-PIN data, incorporating this time the $\dot{P}$ term. We defined the period P_0 as the value at the middle point of the observation, and scanned it over the same joint error range as defined by equations (3) and (4). The analysis was first conducted assuming no phase modulation ($A = 0$). However, the pulse significance did not increase significantly; instead, the X value decreased from equation (5) as $|\dot{P}|$ increased. Thus, a loose limit was obtained as $-1.5 \times 10^{-10} < \dot{P} < 3.2 \times 10^{-10}$ s s^{-1}. We next fixed $T = 36$ ks, and examined the parameter region around equation (10). However, the pulse significance did not increase, either. The obtained limit is again uninteresting, $-1.1 \times 10^{-10} < \dot{P} < 0.8 \times 10^{-10}$ s s^{-1}. In short, period derivatives cannot explain the observed pulse-phase modulation effects.

4.1.3 Non-periodic origin

Another possibility is that the hard X-ray pulse profile (including its phase) is fluctuating randomly for some unspecified reasons, and the variability power happened to be high at $T \sim 36$ ks. To help examine this case, the wave number $q \equiv 86$ ks$/T$ is drawn in blue at the top of figure 4d. Thus, the significant excess in $X_{pk} \equiv Z_2^2$ above

equation (5), e.g., $X_{pk} > 30$, is confined to a rather narrow range of the wave number, $q = 2.4 \pm 0.5$, in good agreement with figure 3c and equation (7). Furthermore, we have already confirmed in sub-subsection 3.2.2 that the power enhancements at $q = 2$ and $q = 3$ in figure 3c are 3σ effects. These facts together mean that the phenomenon should be regarded as periodic rather than random.

There is additional evidence arguing against random phase fluctuations, at least for $10 < T < 30$ ks. In this range, the 15–40 keV X_{pk} values in figure 4d are comparable to X_0, and are all found at $A < 0.15$ s, implying that the pulse significance *diminishes* by demodulation with T in this range. Over a longer period range of $30 < T < 50$ ks, X_{pk} in figure 4d is obtained at $A = 0.5$–0.6 s, as a simple continuation from equation (10). At $T > 50$ ks, the values of A become rather poorly constrained because of the insufficient data length compared to T. Nevertheless, the pulse-phase modulation is not likely to contain significant power at these long periods, either, because the power spectrum in figure 3c shown in red is not enhanced at $q = 1$ above the Poissonian contribution. Therefore, the pulse-phase modulation is unlikely to have a "pink noise" nature including secular changes, which would usually contain significant power at $q = 1$.

To assess the above issue yet from another aspect, we applied the demodulation analysis separately to the first and second halves of the 15–40 keV HXD data. The procedure is the same as in sub-subsection 3.2.3, except that $T = 36.0$ ks was kept fixed because of the shorter data length. Then, the first half gave the significance peak with $X_{max} \equiv X_{pk}(36) = 32.4$ at $A = 0.58 \pm 0.18$ s and $\phi = 272° \pm 18°$, while the second half yielded $X_{max} = 22.7$ at $A = 0.42 \pm 0.17$ s and $\phi = 293° \pm 30°$. In terms of the parameter (A, ϕ), the two halves agree within errors with each other, and with equation (10). Thus, the 36 ks pulse-phase modulation is considered to have persisted through the present observation.

Finally, figure 10 shows the 15–40 keV pulse profiles in the first and second halves of the data, demodulated using the common set of parameters given by equation (10). In fact, we discarded the initial 14 ks of the first half and the final 14 ks of the second half, to make them both represent exactly the time period of 36 ks. Within the photon count fluctuations, the two profiles agree with each other, with $\chi^2 = 0.78$ for $\nu = 12$ (calculated before applying the running average). Thus, the pulse profiles from the first and second modulation cycles, when demodulated using the common set of parameters, become consistent with each other.

In conclusion, we can regard the phase variations in the hard X-ray pulses as periodic, in spite of the rather limited data span.
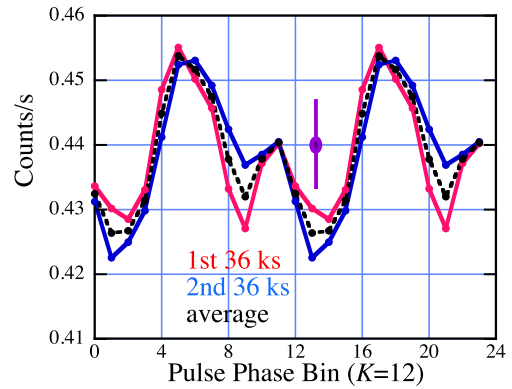

Fig. 10. The 15–40 keV pulse profiles in the first (red) and second (blue) 36 ks, both demodulated using the parameters in equation (10) and folded at equation (4). Their average, shown in dotted black lines, can be slightly different from the red data in figure 2d because of the exclusion of some fraction of the data (see text).

4.2 Interpretation as free precession

4.2.1 Free precession

Let us hereafter limit our interpretation to *periodic* celestial effects. The simplest of these is binary motion of the magnetar; indeed, $A = 0.5$ s and $T = 36$ ks can be explained if the putative companion star has a mass of the order of 0.1 solar mass (depending on the inclination). However, even putting aside the astrophysical reality of such a binary, the absence of the phase modulation in soft X-rays (figure 9) clearly rules out this interpretation, just as in 4U 0142+61.

From the above arguments, free precession (Carlini & Treves 1989; Heyl & Hernquist 2002; MEA14) as described in section 1 remains the most promising possibility. In this scenario, we identify $\hat{x}_3$ with the dipole magnetic axis, assume that it is tilted from $\vec{L}$ (i.e., $\alpha \neq 0$), and consider that the NS is deformed to have a non-zero value of $\epsilon = \Delta I/I$. Then, P_{rot} and P_{prec}, which were degenerate when $\epsilon = 0$, split into two slightly different values according to equation (1). Of these, P_{prec} around $\vec{L}$ is observed as the pulse period of equations (3) and (4), i.e., $P_{prec} = P_0$, while P_{rot} around $\hat{x}_3$ cannot be detected when the emission pattern is symmetric around $\hat{x}_3$ even if $\epsilon \neq 0$ and $\alpha \neq 0$ both hold. This case is thought to apply to the soft component, because it is presumably thermal emission from the NS surface, and should be symmetric around the magnetic axis along which the heat will flow.

If, in contrast, the emission pattern breaks symmetry around $\hat{x}_3$, the observed signals would depend not only on the direction of $\hat{x}_3$ as seen from us, but also on the NS's rotation angle around $\hat{x}_3$ relative to the $\vec{L}$–$\hat{x}_3$ plane. Since this relative angle changes with the slip period T of equation (2), the pulse phase becomes modulated at T (MEA14). With a natural identification of T with the modulation period of 36 ks, this case can explain the behavior of
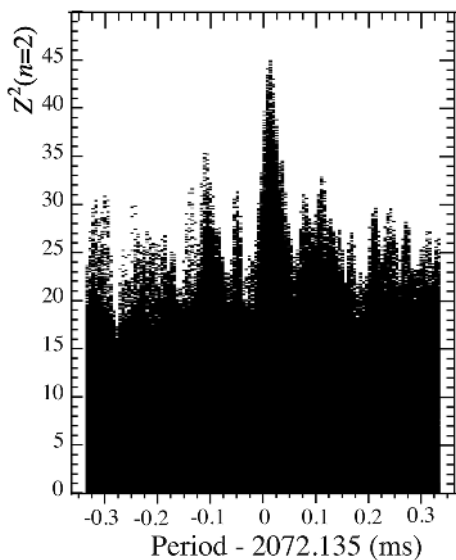
Fig. 11. All the 15–40 keV periodograms obtained in computing figure 4, superposed onto a single plot. The two periodograms in figure 1b are both included here.

the hard X-ray component, and hence equation (2) yields

$$|\epsilon| = |\Delta I/I| = P_0/T = \left(0.58^{+0.04}_{-0.07}\right) \times 10^{-4}. \tag{17}$$

4.2.2 Double periodicity

If the above interpretation is correct, we should be able to observe periodicity also at $P_{\mathrm{rot}} = P_{\mathrm{prec}}/(1 + \epsilon)$. From equation (17), it should appear as a *prograde* period at

$$P^+_{\mathrm{rot}} = 2072.027 \pm 0.014 \,\mathrm{ms} \tag{18}$$

if the deformation is prolate ($\epsilon > 0$), and as a *retrograde* period at

$$P^-_{\mathrm{rot}} = 2072.267 \pm 0.014 \,\mathrm{ms} \tag{19}$$

if oblate ($\epsilon < 0$), although they could appear simultaneously. Of these, P^+_{rot} is already visible in figure 1b. Nevertheless, the issue deserves further examination, because the periodicity at P_{rot} would also be subject to the phase modulation at T, and the significance would change by the demodulation procedure.

Figure 11 shows all the periodograms obtained while computing figure 4, superposed onto a single plot. In addition to the main peak coincident with equation (4), the results thus reveal clear enhancements at $\sim$2072.03 ms and $\sim$2072.25 ms. Since they can be readily identified with P^+_{rot} and P^-_{rot}, respectively, our expectation has been confirmed. Furthermore, the P^+_{rot} peak is somewhat more significant, in agreement with our assumption that the object has a prolate form. To more quantitatively assess the significance of

these two enhancements and their differences remains our future study.

4.3 Comparison with 4U 0142+41

In terms of free precession of an axisymmetric NS, let us compare 1E 1547.0−5408 and 4U 0142+41 (MEA14). The most important feature common to them is the similar degree of deformation, $\epsilon = 1.6 \times 10^{-4}$ in 4U 0142+41 and $\epsilon = 0.6 \times 10^{-4}$ in 1E 1547.0−5408 [equation (17)]. This suggests that the deformation in the two objects has a common origin. Another resemblance between them is the decrease of the pulse-phase modulation amplitude towards lower energies; at least in 1E 1547.0−5408, the effect is consistent with being absent in the soft spectral component. As already described in sub-subsection 4.2.1, these properties can be interpreted by considering that the soft component is emitted symmetrically around the stellar magnetic axis, while the hard component breaks that symmetry. This difference suggests that the two spectral components are distinct not only in their spectral shapes, but also in their emission patterns and/or emission regions.

While the two sources thus show similar behavior, they also exhibit the following three differences, which must be explained in order to further solidify the interpretation.

(1) While we measured $A/P_0 = 0.08 \pm 0.04$ in 4U 0142+61, the ratio is much higher, $A/P_0 = 0.25 \pm 0.07$ (approximately $\pm 1/4$ pulse cycle) in 1E 1547.0−4508 for energies above 10 keV (figure 9).

(2) While $n = 4$ was needed in 4U 0142+61, $n = 2$ is optimum in 1E 1547.0−45408 (sub-subsection 3.2.4).

(3) The hard X-ray pulsation of 4U 0142+61 in the 2009 Suzaku observation was detected only after the demodulation, whereas that of 1E 1547.0−5408 is significant even before such corrections (Paper I).

Let us consider item 1 first. In 4U 0142+61, the sinusoidal hard X-ray modulation with $A/P_0 = 0.08$ was attributed to positional (or directional) deviations of the X-ray emission region (or direction) from the magnetic poles (or from $\hat{x}_3$). There, the emission pattern was implicitly and without particular reason assumed to be pencil-beam like. In contrast, the case of 1E 1547.0−5408 can be better explained by assuming that the emission reaches us (for simplicity, from a single pole) in a *fan-beam-like* pattern, as illustrated in figure 12. The beam will point to us twice per $P_{\mathrm{prec}} = 2.07$ s, when the pole appears from the rim of the NS, to be called "dawn," and disappears behind it, to be called "dusk." This explains the double-peaked pulse profiles (figures 2 and 7), and the $\sim$$\pm 1/4$ cycle offset of the hard X-ray pulse peaks from those in the soft X-rays (figure 7b).
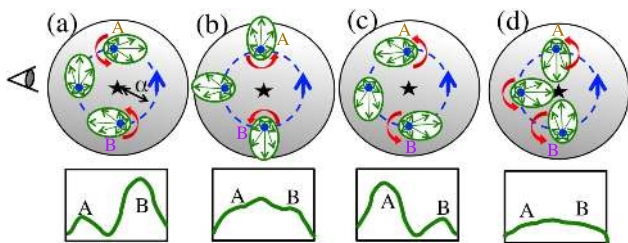
Fig. 12. A possible free precession scenario of an oblate NS, as seen from above onto its angular momentum vector $\vec{L}$ whose tip is represented by a black star. The observer is viewing from the left. The NS's symmetry pole is represented by a small blue circle, and its precession locus by a larger dashed blue circle with a blue arrow. Green ellipses show the hard X-ray emission pattern, which is assumed to be fan-beam like. Panels (a), (b), (c), and (d) represent slip-period epochs of t_0, $t_0 + T/4$, $t_0 + T/2$, and $t_0 + 3T/4$, respectively. A and B indicate "dawn" and "dusk," respectively. The lower panels show the expected hard X-ray pulse profiles.

As already described in section 1 and sub-subsection 4.2.1, we further assume that the fan-beam emission pattern is asymmetric around $\hat{x}_3$. Then, at a certain time t_0 of the 36 ks slip period, the signal will be stronger at the "dusk" pulse phase than at the "dawn" phase, as illustrated in figure 12a; the pulse peak is delayed by $\sim 1/4$ cycle from the average, just as in the red to orange modulation phases in figure 2b. At $t \sim t_0 + T/4$, the configuration will become as in figure 12b, so that the intensity will be similar between "dawn" and "dusk"; the pulse-peak phase will occur at about the "noon" phase with zero delay, as in the yellow profile in figure 2b. Then, at $t \sim t_0 + T/2$, the signal will become strongest at the "dawn" pulse phase, as shown by figure 12c; the pulse peak precedes the average by $\sim P_{\rm prec}/4$, as represented by the green to blue profiles in figure 2b. Finally, at $t \sim t_0 + 3T/4$, the pulse amplitude becomes low, because the emission region is behind the horizon when the beam points towards us; this may correspond to the purple profile in figure 2b. Thus, the fan-beam configuration with broken axial symmetry can explain the large modulation amplitude of 1E 1547.0−5408 reaching $A \sim T/4$. Although the actual configuration (e.g., the contribution from the other pole) would not be as simple as this, more detailed modeling of the emission pattern is beyond the scope of the present paper.

How about the remaining items 2 and 3? In the 2009 data of 4U 0142+61, the hard X-ray pulse profile was richer in fine structures, consisting of three peaks separated by a quarter cycle (figure 1f of MEA14). This is considered to be the reason why $n = 4$ was needed. Moreover, such a complex pulse profile of 4U 0142+61 is thought to have been strongly smeared out by the precession, and hence the hard X-ray pulse was difficult to detect without demodulation, at least in the 2009 Suzaku observation. In contrast, the pulse profiles of the present source are basically double-peaked.

This is considered to make $n = 2$ appropriate for the present source, and make the profile less affected by the phase modulation. In addition, the effects in 1E 1547.0−5408 can be approximated as a sort of pulse-profile change (figure 12), with the "dawn" and "dusk" intensities changing across the slip period, rather than a continuous phase shift. This property is thought to be another factor that has made the pulse easier to detect without demodulation. Thus, the differences in items 2 and 3 can be explained in a qualitative way.

4.4 Relations to other neutron stars

So far, a reasonable number of reports have been made on possible detections of precession from NSs, including accretion-powered objects (e.g., Staubert et al. 2009) and rapidly rotating NSs (e.g., Shabanova et al. 2001; Chukwude et al. 2003; Haberl et al. 2006). However, as discussed in MEA14, such behavior in accretion-powered systems should be regarded as forced precession, because of the strong accretion torque. The fast-rotating NSs can exhibit free precession, because they must be deformed into oblate shapes by centrifugal force. However, the precession would be damped on rather short time scales (Cutler 2002), because an oblate body attains its minimum energy at $\alpha = 0$ under a constant $\vec{L}$. Therefore, these reports remain generally rather unconvincing.

In contrast to these ordinary NSs, magnetars are expected to more ubiquitously exhibit free precession, because their strong $B_{\rm t}$ will deform them into prolate shapes (Ioka 2001; Cutler 2002; Iokai & Sasaki 2004); their centrifugal deformation (oblate) is negligible, e.g., $|\epsilon| < 10^{-6}$, because of their rather long pulse periods, $P = 2$–11 s. Actually, the present data may favor the prolate ($\epsilon > 0$) case (sub-subsection 4.2.2). In such a prolate magnetar, free precession will spontaneously develop because internal energy dissipation processes, with $\vec{L}$ conserved, will increase α on reasonable time scales (Cutler 2002). (As mentioned in MEA14, decay in α by emission of gravitational waves is negligible.) Therefore, the two necessary conditions, $\epsilon \neq 0$ and $\alpha \neq 0$, can be regarded as almost inherent to magnetars with strong $B_{\rm t}$. Actually, the strong pulsations observed from nearly all magnetars imply $\alpha \neq 0$.

The remaining requirement for the detection of free precession, i.e., the non-axi-symmetric emission pattern of the hard component, is considered more conditional rather than intrinsic. One possibility is that a magnetic pole on $\hat{x}_3$ is magnetically connected to a nearby local multipole, and this connecting region is responsible for the hard X-ray generation. Depending on the detailed magnetic configuration, such radiation may well have the required anisotropy around, and positional offsets from, $\hat{x}_3$. Since the

magnetic configuration of a magnetar may change with time (Thompson & Duncan 1995), e.g., across active states, A can change even though T and α are kept constant. Actually, Kuiper et al. (2012) found significant pulse-profile changes in 1E 1547.0−5408 across the 2009 activity episode. Similarly, the hard X-ray phase modulation of 4U 0142+61, detected in 2009 and reconfirmed in a subsequent observation in 2013 (Makishima 2014), was absent in an earlier Suzaku observation made in 2007 (Enoto et al. 2011; see also MEA14). It is, therefore, of significant interest to clarify whether the phase-modulation amplitude A of 1E 1547.0−5408 has been changing along with its long-term decay after the 2009 activity. Future observations of this object with NuSTAR and ASTRO-H are very important.

4.5 Toriodal magnetic fields

From equations (2) and (17), 1E 1547.0−5408 is concluded to be aspheric by $\epsilon = P_0/T = 0.6 \times 10^{-4}$, which is of the same order as that of 4U 0142+61, 1.6×10^{-4} (MEA14). Then, adopting the magnetic deformation interpretation, these NSs are both inferred via equation (1) to have $B_t \sim 10^{16}$ G. The present result thus gives strong support to the suggestion by MEA14 that magnetars have ultra-intense B_t and are hence deformed to a detectable level.

While 4U 0142+61 is a rather aged magnetar with a characteristic age of $\tau_c = 68$ kyr and $B_d = 1.3 \times 10^{14}$ G, 1E 1547.0−5408 has $\tau_c = 1.4$ kyr and $B_d = 2.2 \times 10^{14}$ G. Even though τ_c of magnetars can be systematically overestimated (Nakano et al. 2015), 1E 1547.0−5408 is clearly a much younger and more active object than the other, as evidenced by its faster rotation and higher activity. The somewhat smaller ϵ of 1E 1547.0−5408 apparently contradicts these facts, and the prospect that magnetars must be consuming their toroidal (or internal), as well as dipole (or external), field energies. Possibly, the B_t vs. B_d ratio may scatter considerably among magnetars. To answer this issue, we clearly need to increase the number of detections of free precession from magnetars.

4.6 The wobbling angle α

Finally, we consider possible values of the wobbling angle α. Unlike ϵ, which can be accurately determined via equation (2), α is rather difficult to unambiguously estimate from the data, because its effects degenerate with those of the radiation anisotropy. Below, some qualitative consideration is carried out.

On one hand, α cannot be close to 0, for the following reasons. First, an aligned rotator with $\alpha \sim 0$ ($\hat{x}_3 \parallel \vec{L}$) would

not show the soft X-ray pulsation, as already noticed in subsection 4.4. Second, α would increase on a reasonable time scale (subsection 4.4). Finally, the dipole field derived from the $\sqrt{P\dot{P}}$ factor is in reality $B_d \sin \alpha$ rather than B_d itself, so $\alpha \sim 0$ would demand too high a value of B_d.

On the other hand, α cannot be close to 90°, either. This is because such an orthogonal rotator would exhibit a very high pulse fraction (unless we are observing from a pole-on direction), contradicting the fact that 1E 1547.0−5408 has a particularly low pulse fraction among the known magnetars. All that can be said at present is that α is likely to be in an intermediate range between 0 and 90°. A more realistic estimate on α will be available in future when we model the hard X-ray emission pattern, and fit its predictions to the actual data.

5 Conclusion

During the 2009 January outburst of 1E 1547−5408, its 2.07 s pulsation exhibited a phase modulation with a period of 36 ks, in the 15–40 keV HXD data as well as in the XIS data at energies above 4 keV. The modulation is consistent with being solely carried by the spectral hard component, while absent in the soft component. These results can be understood by presuming that the NS in this object is exhibiting torque-free precession under a deformation by $\epsilon = 0.6 \times 10^{-4}$, and its hard X-ray emission is asymmetric around the NS's symmetry axis. These results further suggest the presence of intense toroidal magnetic fields of $B_t \sim 10^{16}$ G.

Appendix. Phase-randomized demodulation

The significance of the 36 ks HXD phase modulation described in sub-subsection 3.2.4 was evaluated through a *control* study using the same actual data themselves, rather than via a Monte Carlo method. Let us explain how this was carried out.

For this purpose, we again refer to the two-dimensional array $C(j, k)$ (sub-subsection 3.2.1), into which all the 15–40 keV HXD events have been sorted. The pulse phase and the modulation phase are represented by k and j,

respectively. The Z_n^2 calculation effectively produces a folded pulse profile,

$$D(k) = \sum_{j=0}^{J-1} C(j, k), \qquad (A1)$$

and applies the Fourier transform to $D(k)$. Here, we employ rather large values of J and K, namely $J = 90$ and $K = 360$, to avoid binning issues. The demodulation procedure, instead, executes the summation by shifting the pulse phase, according to equation (8), as

$$D(k) = \sum_{j=0}^{J} C[j, k'(j)] \qquad (A2)$$

with

$$k'(j) = k - K(A/P_{0h}) \cdot \sin(2\pi j/J - \phi). \qquad (A3)$$

Let us assume, as a null hypothesis, that the pulse phase is intrinsically *not* modulated with period T. Then, the demodulation procedure using equations (A2) and (A3) has two effects: (i) to degrade the underlying pulse coherence, and (ii) to add up the Poisson noises of different pixels in various different ways. Large values of X_{max}, as in equation (9), will appear when (ii) overwhelms (i). Importantly, these two effects must remain unchanged even when a random permutation is applied on the rows $\{j = 0, 1, \ldots, J-1\}$, because all rows must be equivalent with respect to (i), and the Poisson noise in different pixels of $C(j, k)$ should be mutually independent when considering (ii).

With the above in mind, we repeated the same demodulation search 1000 times, over the same (P, T, A, ϕ) volume. In each trial, $k'(j)$ in the above two equations were replaced with $k'(j')$, where $\{j' = 0, 1, \ldots, J-1\}$ is a random permutation of $\{j = 0, 1, \ldots, J-1\}$. Different trials employed different realizations of the permutation, all with $J = 90$. We thus obtained 1000 values of X_{max}, of which the histogram is shown in figure 5a. By integrating this distribution from $X_{max} = +\infty$ towards lower values of X_{max}, the upper probability integral has been obtained as in figure 5b. This gives the chance occurrence probability of large values of X_{max}, under the presence of the pulsation at P_0 but the absence of any intrinsic periodicity at T. Equation (11) provides its approximation at $X_{max} > 35$.

This control study is considered to be rather conservative for the following reasons. When the phase modulation is sinusoidal, a small difference in the initial value of ϕ will not affect X, because Δt is expected to have a long coherence length in ϕ. This makes a scan over ϕ only partially independent. However, when the random permutation is employed, Δt attains a rather short (typically, $2\pi/J$ radians)

coherence in ϕ, so that scans over ϕ all become essentially independent. As a result, one control run is expected to involve effectively a larger number of trials. If this effect is taken into account, the true chance probability would be even lower than equation (11).

References

Beloborodov, A. M., & Thompson, C. 2007, ApJ, 657, 967
Braithwaite, J. 2009, MNRAS, 397, 763
Brazier, K. T. 1994, MNRAS, 268, 709
Buccheri, R., et al. 1983, A&A, 128, 245
Butikov, E. 2006, Euro. J. Phys., 27, 1071
Carlini, A., & Treves, A. 1989, A&A, 215, 283
Chukwude, A. E., Ubachukwu, A., & Okeke, P. 2003, A&A, 399, 231
Cutler, C. 2002, Phys. Rev. D., 66, 084025
Dall'Osso, S., Shore, S. N., & Stella, L. 2009, MNRAS, 398, 1869
den Hartog, P. R., Hermsen, W., Kuiper, L., Vink, J., in't Zand, J. J. M., & Collmar, W. 2006, A&A, 451, 587
Enoto, T., et al. 2010a, PASJ, 62, 475 (Paper I)
Enoto, T., Makishima, K., Nakazawa, K., Kokubun, M., Kawaharada, M., Kotoku, J., & Shibazaki, N. 2011, PASJ, 63, 387
Enoto, T., Nakazawa, K., Makishima, K., Rea, N., Hurley, K., & Shibata, S. 2010b, ApJ, 722, L162
Enoto, T., Nakagawa, Y. E., Sakamoto, T., & Makishima, K. 2012, MNRAS, 427, 2824
Gelfand, J., & Gaensler, B. M. 2007, ApJ, 667, 1111
Haberl, F., Turolla, R., De Vries, C. P., Zane, S., Vink, J., Méndez, M., & Verbunt, F. 2006, A&A, 451, L17
Harding, A., & Lai, D. 2006, Rep. Prog. Phys., 69, 2631
Heyl, J. S., & Hernquist, L. 2002, ApJ, 567, 510
Ioka, K. 2001, MNRAS, 327, 639
Ioka, K., & Sasaki, M. 2004, ApJ, 600, 296
Iwahashi, T., Enoto, T., Yamada, S., Nishioka, H., Nakazawa, K., Tamagawa, T., & Makishima, K. 2013, PASJ, 65, 52
Kokubun. M.,, et al.2007, PASJ, 59, S53
Koyama, K., et al. 1989, PASJ, 41, 461
Koyama, K., et al. 2007, PASJ, 59, S23
Kuiper, L., Hermsen, W., den Hartog, P., & Collmar, W. 2006, ApJ, 645, 556
Kuiper, L., Hermsen, W., den Hartog, P. R., & Urama, J. O. 2012, ApJ, 748, 133
Landau, L. D., & Lifshitz, E. M. 1976, Mechanics, 3rd ed., vol. 1 (Oxford: Butterworth-Heinemann), ch. 4.
Makishima, K. 2014, Abstract, in The European Week of Astronomy and Space Science (EWASS), Special Session 1, 287
Makishima, K., Enoto, T., Hiraga, J. S., Nakano, T., Nakazawa, K., Sakurai, S., Sasano, M., & Murakami, H. 2014, Phys. Rev. Lett. 112, 171102 (MEA14)
Mereghetti, S. 2008, A&AR, 15, 225
Mitsuda, K., et al. 2007, PASJ, 59, S1
Nakano, T., Murakami, H., Makishima, K., Hiraga, J. S., Uchiyama, H., Kaneda, H., & Enoto, T. 2015, PASJ, 67, 9
Rea, N., et al. 2012, ApJ, 754, 27
Rea, N., et al. 2013, ApJ, 770, 65

Rea, N., Vigan, D., Israel, G. L., Pons, J. A., & Torres, D. F. 2014, ApJ, 781, L17

Ruderman, M., & Gil, J. 2006, A&A, 460, L31

Shabanova, T. V., Lyne, A. G., & Urama, J. O. 2001, ApJ, 552, 231

Staubert, R., Klochkov, D., Postnov, K., Shakura, N., Wilms, J., & Rothschild, R. E. 2009, A&A, 494, 1025

Takahashi, T., et al. 2007, PASJ, 59, S35

Takiwaki, T., Kotake, K., & Sato, K. 2009, ApJ, 691, 1360

Terada, T., et al. 2008, PASJ, 60, 387

Thompson, C., & Duncan, R. C. 1995, MNRAS, 275, 255

Tiengo, A., et al. 2013, Nature 500, 312

Vink, J., & Kuiper, L. 2006, MNRAS, 370, L14